*metals*

MDPI

*Article*

# Fatigue Damage in Shot-Peened Al7075-T6 Alloy: Correlation Between Acoustic Emission Spectra and Fractographic Analysis

**Matteo Benedetti [1], Vigilio Fontanari [1,*], Emiliano Rustighi [1], Pasquale Gallo [1] and Michele Bandini [2]**

[1] Department of Industrial Engineering, University of Trento, Via Sommarive 9, 38123 Trento, Italy; matteo.benedetti@unitn.it (M.B.); emiliano.rustighi@unitn.it (E.R.); pasquale.gallo@unitn.it (P.G.)
[2] PeenService srl, Via Pollastri 7, 40138 Bologna, Italy; m.bandini@peenservice.it
* Correspondence: vigilio.fontanari@unitn.it

**Abstract**

Shot-peening treatments improve the fatigue performance of mechanical components thanks to the surface modifications introduced and mainly due to the residual compressive stresses present in the layer of material near the shot-peened surface. There is no unanimous agreement in scientific literature regarding the kinetics of the damage process. However, it is generally accepted that, due to morphological and microstructural changes in the shot-peened layer, the material is more prone to early crack initiation, the propagation of which is then significantly slowed down or even stopped by the local stress field. This work focuses on applying the acoustic emission (AE) technique to detect fatigue crack initiation and propagation in shot-peened Al-alloy components. The analysis is conducted on Al-7075-T6 alloy, subjected to different shot-peening conditions and fatigue tested under alternating four-point bending. The results from the AE analyses are then correlated with a fractographic analysis. For all shot-peening conditions investigated, acoustic emission consistently indicated probable crack nucleation at approximately two-thirds of the total fatigue life, followed by a significant damage accumulation phase prior to dominant crack propagation. The final increase in acoustic activity coincided with the measurable loss of stiffness, confirming the onset of accelerated crack growth leading to fracture. The results demonstrate that, despite some experimental challenges, AE monitoring has the potential for the early detection of damage initiation.

**Keywords:** acoustic emission; shot-peening; 7075 Al-alloy; high-cycle fatigue; fracture; crack initiation; crack propagation



Academic Editors: Dariusz Rozumek and Grzegorz Lesiuk

Received: 26 February 2026
Revised: 14 March 2026
Accepted: 18 March 2026
Published: 19 March 2026



## 1. Introduction

Shot-peening treatment is generally used to enhance the fatigue response of mechanical components, mainly due to residual compressive stresses that are introduced into a surface layer whose thickness depends on the material and the treatment intensity [1–3]. In certain situations, surface modifications that produce strain hardening also contribute to improving fatigue response [2,4,5]. More generally, especially for high shot-peening intensity conditions, the literature reports a negative effect following the local accumulation of plastic deformation energy. This accumulation produces a very unstable dislocation structure [6,7], which is naturally predisposed to evolve towards conditions that trigger fatigue cracks. The modifications of the surface morphology, characterized by increased roughness associated with higher shot-peening intensities, lead to harmful local stress concentration effects [8–10]. The concomitant effect of the residual stress field, microstructural changes,

and deterioration of the surface morphology produces different outcomes depending on the shot-peened material [7,10–12]. It should also be noted that in some types of material, the treatment induces the transformation of metastable phases (e.g., mechanically induced martensitic transformation) with a beneficial effect on the microstructure and the residual stress field [13–15].

Aluminum alloys, especially the high-performance ones (e.g., aeronautical applications alloys belonging to the 7000 series), have favorable specific strength parameters but generally exhibit rather low fatigue resistance [16,17]. For this reason, they have been the focus of extensive experimental campaigns aimed at identifying optimal shot-peening conditions to improve the surface fatigue performance of components. Summarizing the main results and contributions, it can be said that this class of alloys tolerates light or medium-intensity shot-peening conditions, while suffering from the intense deformations produced by high-intensity or prolonged treatments [18–21]. The improvement in fatigue response due to the residual stress field is strongly influenced by microstructural changes and significant variations in surface roughness.

There is no agreement in the literature regarding the evolution of fatigue damage in shot-peened components. In particular, the loading conditions may alter the residual stress field, leading to relaxation of compressive stresses and a consequent reduction in their barrier effect against crack propagation [22,23]. This aspect is quite common for high-stress conditions in medium to low cycle fatigue regimes, where the improving effect of the treatment compared to the untreated condition is negated. The improvements are more evident in high-cycle fatigue conditions, when the stress level is such that the barrier effect due to residual compressive stresses can be fully exploited. There is evidence in the literature of situations in which the residual stress field completely blocks the evolution of damage from the surface and fatigue cracks initiate below the surface, in regions where the compressive stress profile rapidly evolves towards very small values or even towards values of limited tensile conditions [24–27]. This effect, which is less frequent for notched components characterized by a strong stress gradient at the root of the notch, can instead become competitive with surface damage under conditions of uniform stress on the section, given the limited depth of the modified surface layer. Surface initiation is generally favored for the most critical deformation conditions near the free surface: increased microstructural entropy and plane stress state. Subsurface initiation is mostly activated in the presence of internal defects such as pores or inclusions. For aluminum alloys, the production process generally leads to microstructural conditions with little evidence of potentially harmful defects. Therefore, a predominance of surface-type initiation should be expected, although the concurrence of initiation modes cannot be ruled out, as observed in several contributions [28,29]. It remains unclear under which conditions these triggering factors arise and what fraction of the fatigue life is consumed in the initiation of one or more critical cracks that subsequently propagate to failure.

It becomes clear that a reliable method capable of tracking damage evolution during fatigue loading would therefore be highly beneficial to experimentally investigate those phenomena.

In this context, the acoustic emission (AE) technique appears particularly promising, as it enables real-time monitoring of the acoustic waves generated by energy-releasing phenomena within the material. These phenomena may be macroscopic, such as crack growth, plastic deformation, or local debonding of inclusions, precipitates, or dispersed phases, as well as microscopic events, including void nucleation and dislocation motion within the crystal lattice [30–34].

The AE signal is characterized by a wavefront of variable amplitude and duration that can be related to the energy released by the ongoing damage process.

Generally, during the damage process, sequences of events with very different characteristics are detected. It is therefore not easy to associate these events with the process in progress. Nevertheless, from the analysis of certain parameters, such as the counting of peaks above a specific threshold, the maximum amplitude reached, the absolute energy associated with the event, and the evolution over time of the number of significant events, it is possible to derive an interpretative key of damage evolution. Figure 1 shows the salient features of the wavefront, typically in a frequency range between 100 and 500 kHz, produced by irreversible internal phenomena and detected by sensors in contact with the component.

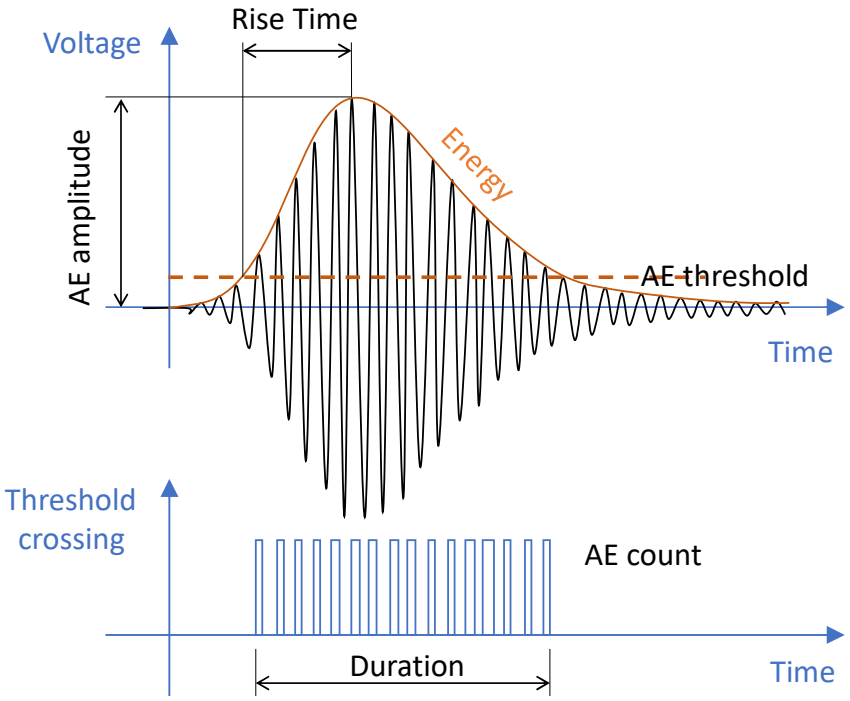


**Figure 1.** Essential descriptive parameters of an AE wavefront.

There are notable examples in the literature of the use of AE for studying crack propagation during static and dynamic testing. The technique is very useful and often provides easily interpretable information [33,35–37]. In describing the phenomenon of fracture and fatigue fracture, the technique is very sensitive for monitoring the propagation of mechanically long cracks, and therefore it has been used successfully in the interpretation of the results of fracture mechanics and fatigue crack propagation tests [29,34,38]. There are far fewer studies on the conditions that lead to the initiation of fatigue cracking and their subsequent propagation starting from mechanically and microstructurally short cracks. In these cases, the swarm of acoustic events is very often masked by noise sources that are not always easily identifiable [39–41]. Some studies highlight how the value of the information that can be deduced from AE spectra increases significantly when discussed in parallel with damage parameter measurements obtained using other detection techniques, also considering the possibility of training physically informed neural networks [42–45].

Against this background, this paper addresses precisely this issue. Since the presence of cracks ab origine is not known in the shot-peened component, the AE method is employed to determine whether a threshold condition can be identified, at which a crack becomes clearly detectable, allowing its propagation to be monitored. Particular attention is devoted to the relationship between crack development and the residual compressive stress field on the surface. Specifically, the aim is to assess the minimum identifiable crack

size in relation to the depth of the residual stress profile and its location, whether at the surface or within the bulk material unaffected by the treatment.

The experiments are conducted on Al 7075-T6 aluminum alloy specimens subjected to different peening conditions and subsequently tested for fatigue with alternating four-point bending tests.

The work is organized as follows: Section 2 describes the material, treatments, fatigue test conditions, and experimental setup for measuring acoustic emissions; Section 3 reports the main experimental results, discusses the set of acoustic events measured on the different specimens in relation to the treatment conditions and fatigue results and analyzes the results of the fractographic analysis conducted on specimens for which the test was interrupted at the first evidence of a significant acoustic event; Section 4 summarizes the results obtained and reports the main conclusions.

## 2. Materials and Methods

The experiments were conducted on Al7075-T6 alloy. The static tensile properties of the material are summarized in Table 1.

**Table 1.** Material properties.

| Young Modulus [MPa] | Yield Strength [MPa] | UTS [MPa] | True Fracture Strength [MPa] |
|---|---|---|---|
| 72 | 505 | 570 | 760 |

For the experimental investigation, hourglass shape samples with circular section samples were used, as presented in Figure 2. A large curvature radius was imposed so that notch effect was negligible.

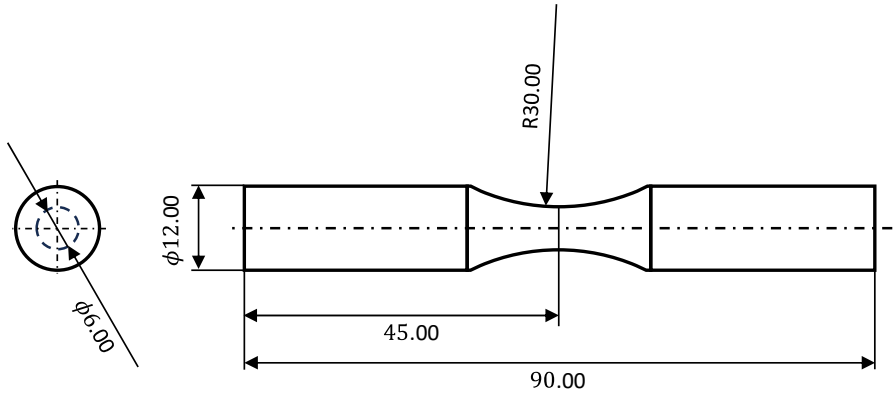


**Figure 2.** Geometry of test samples (dimensions in mm).

The samples, divided into batches of approximately 20 specimens, were subjected to different shot-peening treatments. Parameters of the treatments are summarized in Table 2. As a benchmark, one batch of specimens was kept in the unpeened condition.

**Table 2.** Shot peening treatment conditions.

| Treatment | Shots/Diameter [μm] | Intensity | Coverage (%) |
|---|---|---|---|
| UFS50 | Steel/50 | 10–12 N | 100 |
| Z100/1000 | Ceramic/100 | 8–10 N | 1000 |
| Z100 | Ceramic/100 | 10–12 N | 100 |
| Z425 | Ceramic/425 | 4–6 A | 100 |
| Z425 + Z100 | Ceramic/425-100 | 4–6 A + 8–10 N | 100 + 1000 |

The shot-peening treatments were selected to generate markedly different surface integrity conditions, allowing the individual contributions of the main shot-peening-induced mechanisms to be investigated. In particular, the treatments were designed following the rationale discussed in previous investigations on Al alloys, where different combinations of shot size, intensity, and coverage are used to emphasize specific fatigue-related effects such as residual compressive stresses, surface roughness, work hardening, and possible microstructural refinement of the surface layer. The light treatments (UFS50 and Z100) employ relatively small shots and moderate intensity, producing shallow compressive residual stress profiles while limiting the increase in surface roughness. Such conditions are generally considered favorable for high-strength aluminum alloys, which can be sensitive to excessive plastic deformation. In contrast, the treatment performed with larger ceramic shots (Z425) introduces a deeper compressive residual stress field but is also associated with stronger surface deformation and higher roughness levels. A high-coverage treatment (Z100/1000) was also considered to promote more intense plastic deformation in the near-surface region, potentially leading to microstructural refinement and enhanced work hardening. Finally, a combined treatment (Z425 + Z100) was included to reproduce a double-peening strategy in which an initial high-intensity treatment generates a deep compressive stress profile, while a subsequent treatment with smaller shots partially improves the surface morphology and modifies the near-surface stress distribution.

To give the reader an overview of the effects produced by these treatments, the main results are summarized in Table 3. Further detailed information and images of the resulting surface morphology can be found in [20]. The table reports, for each treatment variant, the surface roughness parameters (Ra: average roughness; Rq: root mean square roughness), the microhardness values measured near the treated surface, the peak value of the residual compressive stress ($\sigma_{RS,min}$), the distance of this peak from the shot-peened surface ($\delta_{RS,min}$), and the overall depth of the residual stress profile ($\delta_{Rs}$).

**Table 3.** Main parameters describing the effect of the surface treatments.

| Treatment | Ra (μm)/Rq (μm) | Microhardness (HV0.025) | $\sigma_{RS,min}$ [MPa]/$\delta_{RS,min}$ (mm) | $\delta_{RS}$ (mm) |
|---|---|---|---|---|
| As received | 0.87/1.04 | 173 | - | - |
| UFS50 | 1.16/1.47 | 185 | 175/0.025 | 0.080 |
| Z100/1000 | 1.36/1.71 | 174 | 200/0.028 | 0.008 |
| Z100 | 1.34/1.72 | 174 | 255/0.028 | 0.08 |
| Z425 | 2.15/2.66 | 165 | 250/0.025 | 0.18 |
| Z425 + Z100 | 2.04/2.59 | 176 | 225/0.100 | 0.21 |

For residual stresses, the first three treatments listed in Table 2 produce profiles with a similar penetration depth (approximately 80 μm), although they differ in terms of peak compressive stress values. In contrast, the high-intensity treatment and the combined treatment generate significantly deeper residual stress profiles, reaching depths of approximately 200 μm, while the peak compressive stresses tend to approach a saturation value of about 250 MPa. Owing to the different peening intensities and process conditions, noticeable differences in surface morphology and microstructural features are also observed, as documented in detail in the referenced study [20].

The fatigue tests were conducted on the Rumul Mikroton 20 kN resonant testing machine, in the alternating four-point bending configuration (R = −1) shown in Figure 3. The sensor for detecting acoustic emissions was positioned at the base of the specimen as indicated in the figure. The sensor is a Mistras AE Micro 80 [46] operating in the 40–400 kHz frequency range, with a sampling frequency of 1 MPS. AE acquisition took place for 36 of

the 95 specimens tested. Based on preliminary analyses conducted under very-low-load conditions, a threshold of 30 dB was defined as the limit for identifying the acoustic signal.

The tests explored a fatigue life range between $6 \times 10^4$ and $2 \times 10^7$ cycles. Specimens that survived this upper limit are considered run-out and are marked with a horizontal arrow in the fatigue graph. Based on the stiffness of the test setup, fatigue tests were conducted at a resonance frequency of approximately 91 Hz. The test frequency changes with the evolution of the specimen stiffness as the crack grows and therefore becomes a parallel system for detecting damage propagation. For this reason, the resonant frequency was acquired during the test until fracture and reported in parallel with the information obtained from the AE spectra.

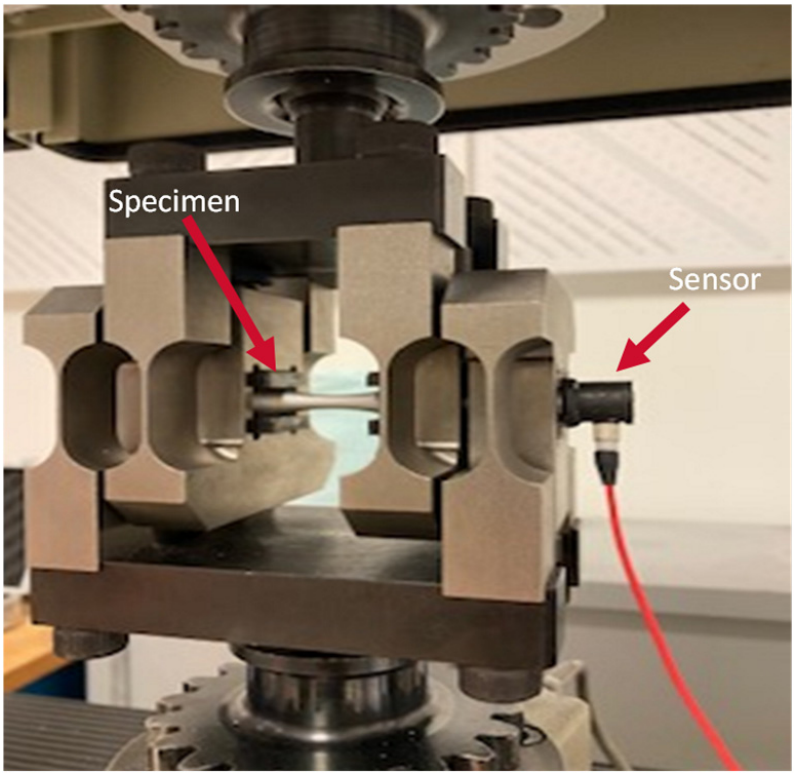


**Figure 3.** Test setup; the sensor is attached to the base of the test specimen.

For some selected specimens, based on the information obtained from the AE spectra recorded in tests carried out at the load levels during the experimental campaign, the fatigue tests were interrupted at the first significant AE event. The specimens were then retested under axial fatigue with a positive load ratio (R) to complete the fracture. This procedure was adopted to mark the crack front associated with the detected acoustic activity and to maintain the opening of the crack mouth during subsequent propagation. Such marking is essential to confirm the actual occurrence of crack initiation through SEM fractographic analysis.

## 3. Results and Discussion

### *3.1. Fatigue Results*

The results of the fatigue tests are described in detail in [20]. The data are reworked in Figure 4, in which the pinpoints indicate the specimens that were instrumented with the AE sensor during the test. A total of 15 tests was performed for each material condition. The Wöhler's curves were fitted using Equation (1):

$$\sigma_a = c_1 + c_2 N_f^{-c_3} \quad (1)$$

where $c_1$, $c_2$, and $c_3$ are fitting parameters whose values are reported in [20], $N_f$ is the number of cycles upon failure and $\sigma_a$ is the stress amplitude. The scatter bands at 10% and 90% probability of failure, represented by different colors for the variants studied, are calculated considering a uniform regression variance over the entire fatigue life range.

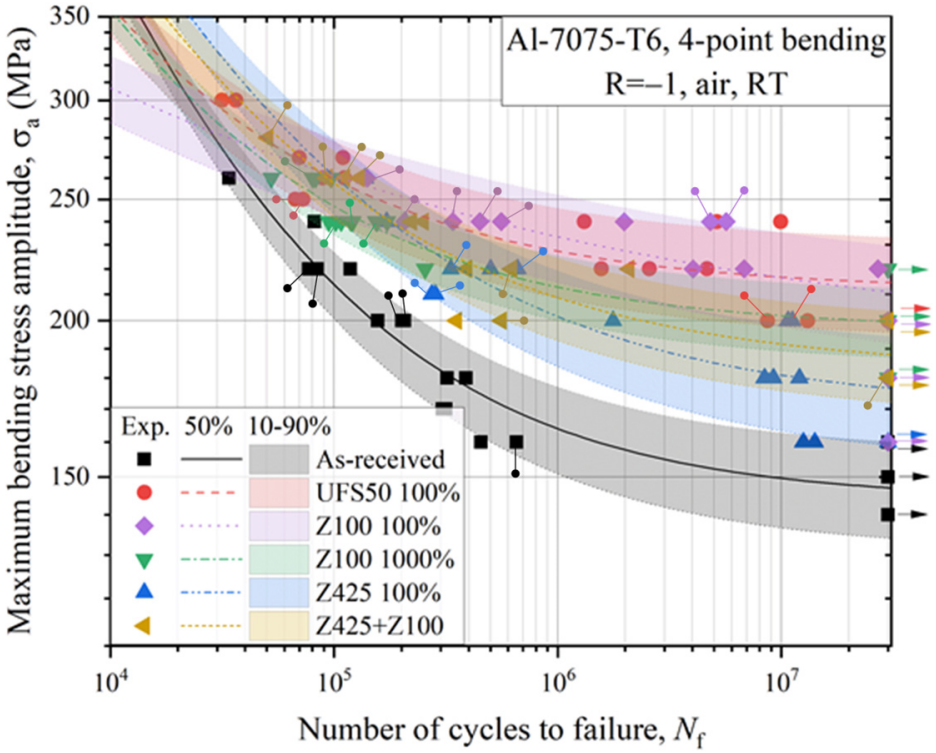


**Figure 4.** Results of the fatigue tests. AE-instrumented specimens are indicated by pinpoints.

All shot-peening variants show an improvement over the untreated condition, more pronounced in the region of high-cycle fatigue, gradually becoming less evident with increased stress amplitude, with up to almost negligible differences at the highest load levels. The two lighter treatments (i.e., UFS50 100% and Z100 100%) achieve the best increase in fatigue response and a lower statistical dispersion of results [20]. The more intense treatment, carried out with larger shot, proves to be less effective, with lower fatigue resistance and greater statistical dispersion of results compared to the other shot-peening variants. This behavior is partly improved in the variant in which, following the heavy treatment, a light treatment is carried out for prolonged periods of time to improve the surface morphology and maintain a deep residual stress profile. However, the improvement obtained does not exceed the results obtained with the less intense treatments.

### *3.2. Acoustic Emission Spectra*

Referring to the representation shown in Figure 1, for each acoustic event, it is possible to extract the maximum amplitude assumed by the signal (AE amplitude), the number of times the amplitude exceeds a threshold level set at 30 dB (AE counts), and, through integration, the energy associated with the event (Energy). In addition, the integral of the events occurring throughout the test normalized with respect to the final cumulative value can be plotted. Exemplary AE spectra collected during the test for these parameters are presented for each of the different variants in Figures 5–10.

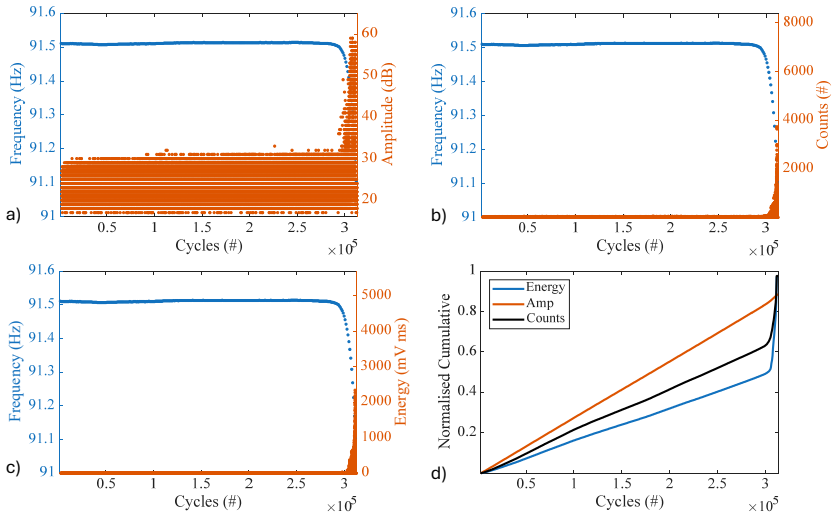


**Figure 5.** Acoustic emission spectra for a specimen stressed of the unpeened variant: (**a**) signal amplitude; (**b**) events counts; (**c**) energy associated with events; (**d**) cumulative normalized graphs.

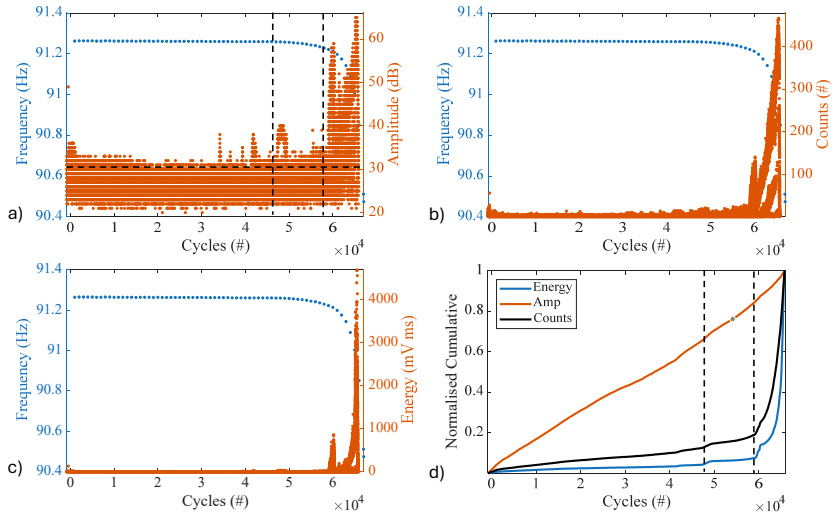


**Figure 6.** Acoustic emission spectra for a specimen stressed of the UFS50 variant: (**a**) signal amplitude; (**b**) events counts; (**c**) energy associated with events; (**d**) cumulative normalized graphs.

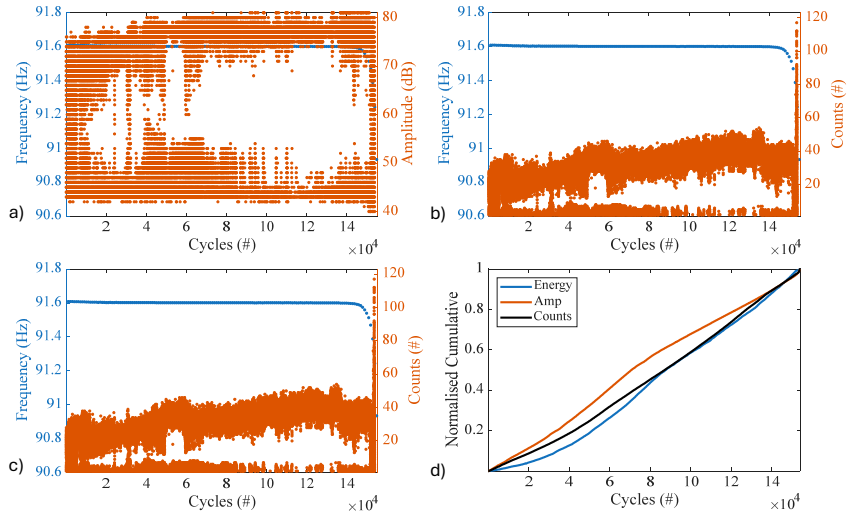


**Figure 7.** Acoustic emission spectra for a specimen stressed of the Z100-1000% variant: (**a**) signal amplitude; (**b**) events counts; (**c**) energy associated with events; (**d**) cumulative normalized graphs.

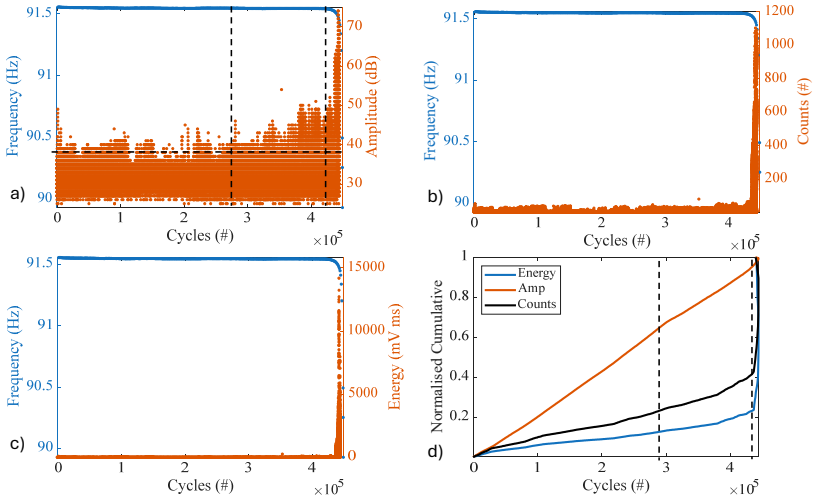


**Figure 8.** Acoustic emission spectra for a specimen stressed of the Z100-100% variant: (**a**) signal amplitude; (**b**) events counts; (**c**) energy associated with events; (**d**) cumulative normalized graphs.

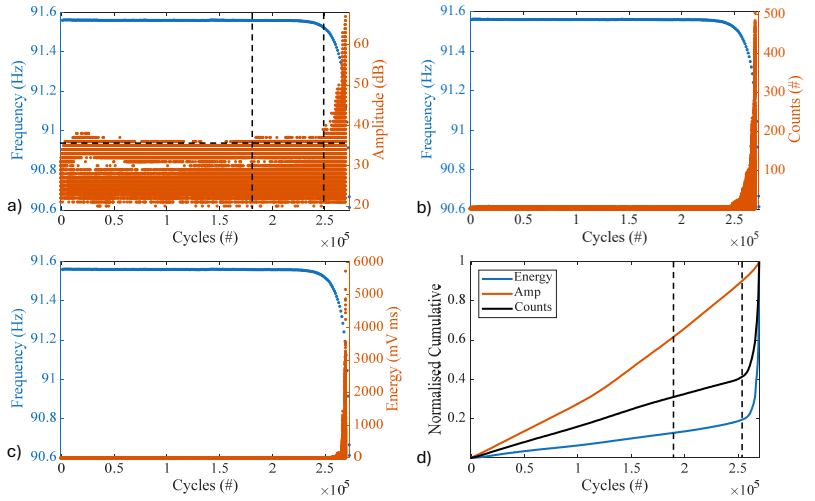


**Figure 9.** Acoustic emission spectra for a specimen stressed of the Z425 variant: (**a**) signal amplitude; (**b**) events counts; (**c**) energy associated with events; (**d**) cumulative normalized graphs.

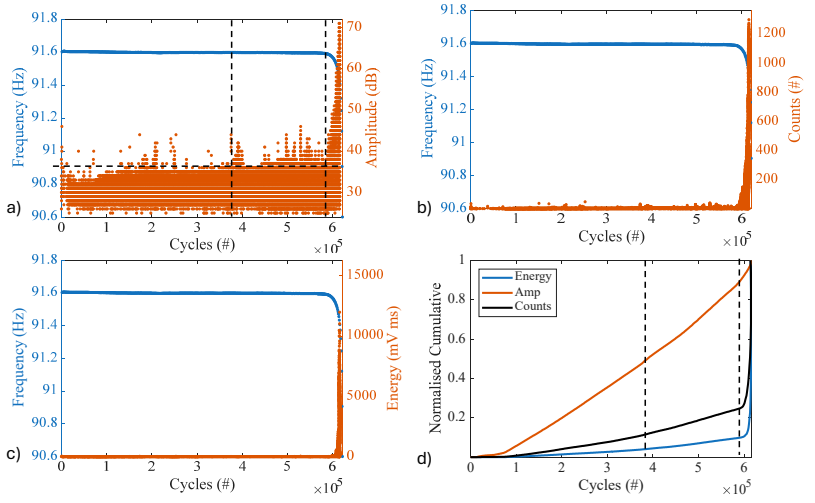


**Figure 10.** Acoustic emission spectra for a specimen stressed of the dual Z425 + Z100 variant: (**a**) signal amplitude, (**b**) events counts, (**c**) energy associated with events, (**d**) cumulative normalized graphs.

The testing machine resonance frequency values recorded during the test are plotted together with the AE spectra. Traces remain nearly constant for most of the life, with a rapid decrease only in the final stages of the test. At this point, there is also a clear increase in acoustic activity.

The acoustic emission spectra acquired may show different trends even for test pieces belonging to the same variant. The response obtained for the three samples of the Z100-1000% variant is very unusual and difficult to interpret. Figure 6 shows a representative trend.

The amplitude spectra and the cumulative curves seem to capture some synthetic aspects of the response. Where possible, the condition in which the amplitude of the events rises steadily above the background signal has been highlighted in the figures. For the sake of clarity, the background signal is around 30 dB, as mentioned before. This condition is accompanied by a somewhat marked change in slope in the cumulative curves and generally occurs around 60% of the entire fatigue life. In the figures, the onset of the final phase of the test (i.e., shortly before the final fracture), in which the acoustic activity significantly increases, is also indicated. In this region, which occupies approximately the last 5% of the entire fatigue life, a steep decrease in the resonance frequency of the test is observed. This decrease is attributable to the loss of stiffness of the specimen due to the propagation of a crack of rapidly increasing size, until final collapse.

The first stable increase in acoustic activity associated with the change in slope of the cumulative curves is indicated in the literature [31,32] as a trigger signal for the initiation of a detectable crack. Subsequently, the crack can propagate steadily or be blocked in the presence of microstructural barriers or barriers linked to residual stress fields, until the final acceleration.

### *3.3. Fractographic Analysis*

Based on observations derived from emission spectra, it was decided to suspend some of the tests at the first significant manifestation of acoustic activity associated with the variation in slope in the cumulative curves. The specimens were then broken by cyclic axial stress at a load ratio $R > 0$, to mark the separation between potential cracks that had already initiated when the test was suspended and their subsequent propagation under cyclic axial test conditions. The fracture surfaces analyzed under an electron scanning microscope (SEM) revealed the presence, near the free surface, of a small region with smooth faces, clearly distinct from the rest of the propagation surface. Some examples of tests carried out for the different material variants are shown in Figures 11–15, which show the entire fractured section and a detail of the region where there is evidence of initial cracking, made clear by overlay due to compression contact between the opposite fracture surfaces during the bending cycle. The separation between what can be interpreted as the flexural initiation region and the subsequent propagation due to cyclic axial stress is highlighted in the figures by a dotted line.

This fractographic characteristic, which occurs in all cases, even for the non-shot-peened variant, may be an indication of the initiation of one or more cracks during the alternating bending stress phase ($R = -1$), which involves compression between the fracture surfaces for half of the applied stress cycle. It can be added, for the shot-peened variants, that near the surface, the state of residual compressive stress contributes to extending the fraction of the load cycle that produces compression between the fracture surfaces. The rest of the fractured surface is compatible with the propagation condition expected for cyclic tests with a load ratio $R > 0$, clearly showing the radial extension of the fracture starting from the initiation sites with an increasingly rough surface until the final condition of fracture due to static overloading.

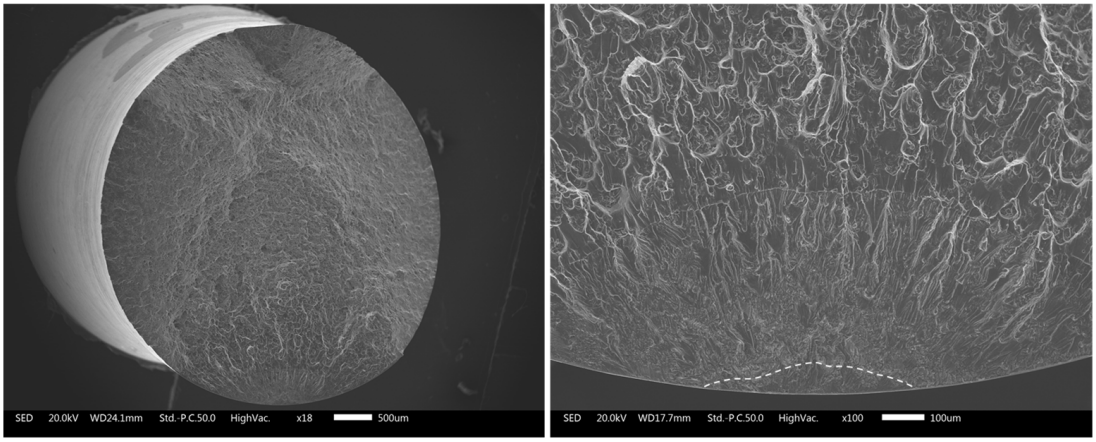


(**a**) (**b**)

**Figure 11.** Fractography of the unpeened variant, subjected to alternating bending stress with amplitude $\sigma_A$ = 170 MPa for 1.1 × $10^5$ cycles and subsequently brought to fracture with axial cyclic testing. (**a**) Fracture surface; (**b**) detail on the initiation site.

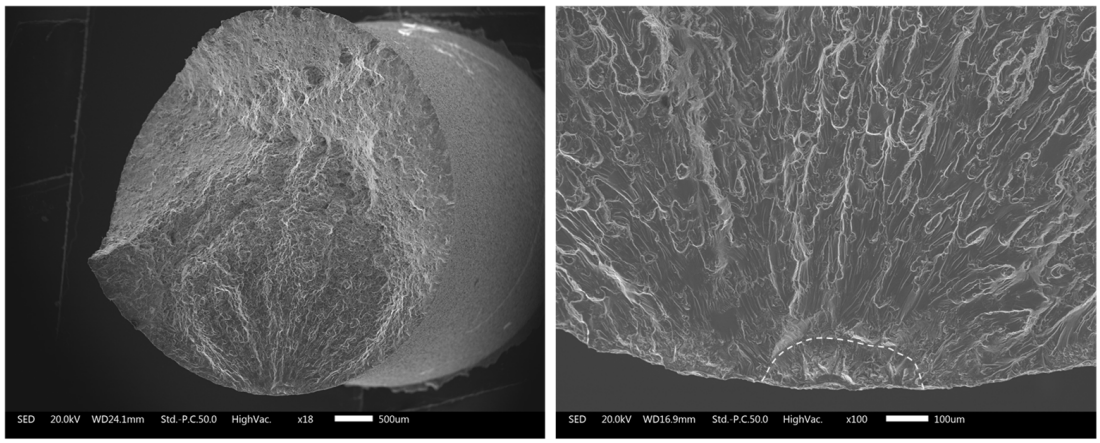


(**a**) (**b**)

**Figure 12.** Fractography of the UFS50 variant subjected to alternating bending stress with amplitude $\sigma_A$ = 250 MPa for 4.0 × $10^4$ cycles and subsequently brought to fracture with axial cyclic testing. (**a**) Fracture surface; (**b**) detail on the initiation site.

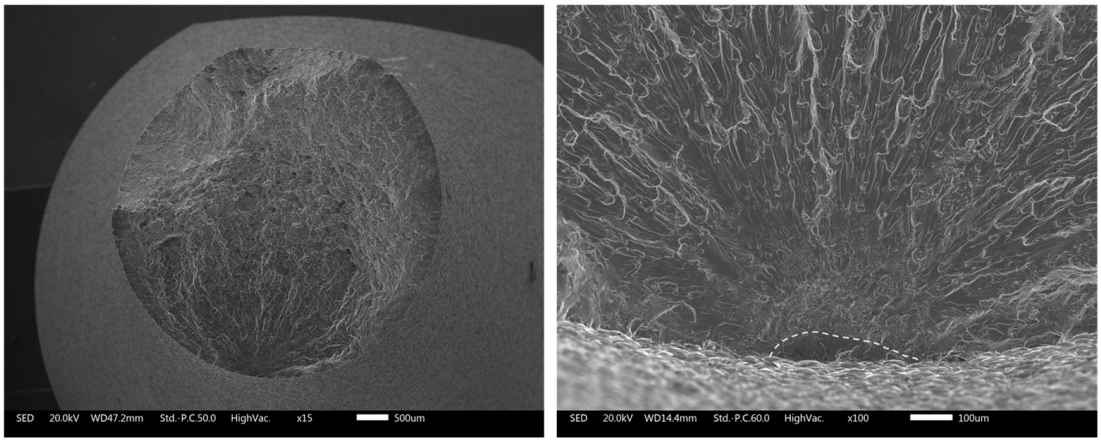


(**a**) (**b**)

**Figure 13.** Fractography of variant Z100-100% subjected to alternating bending stress with amplitude $\sigma_A$ = 260 MPa for 9.5 × $10^4$ cycles and subsequently brought to fracture with axial cyclic testing. (**a**) Fracture surface; (**b**) detail on the initiation site.

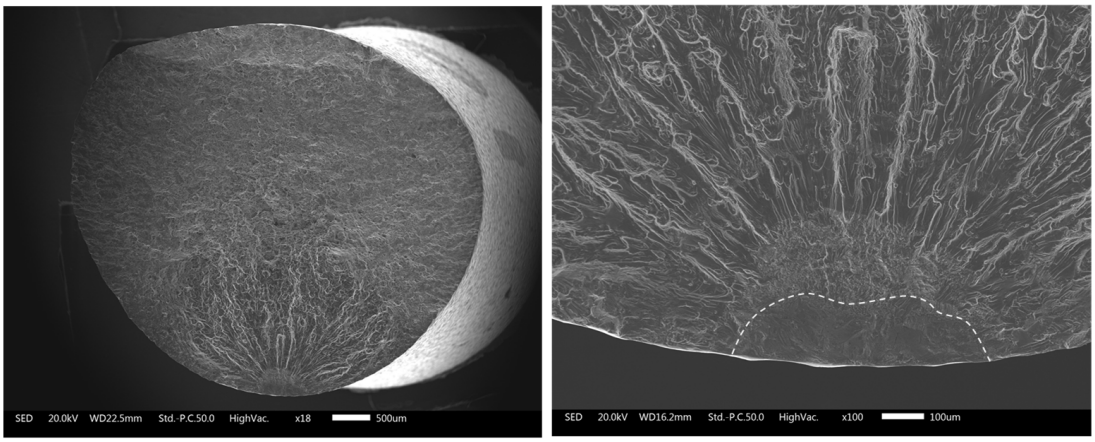


(**a**) (**b**)

**Figure 14.** Fractography of variant Z425-100% subjected to alternating bending stress with amplitude $\sigma_A$ = 260 MPa for 9.5 × $10^4$ cycles and subsequently brought to fracture with axial cyclic testing. (**a**) Fracture surface; (**b**) detail on the initiation site.

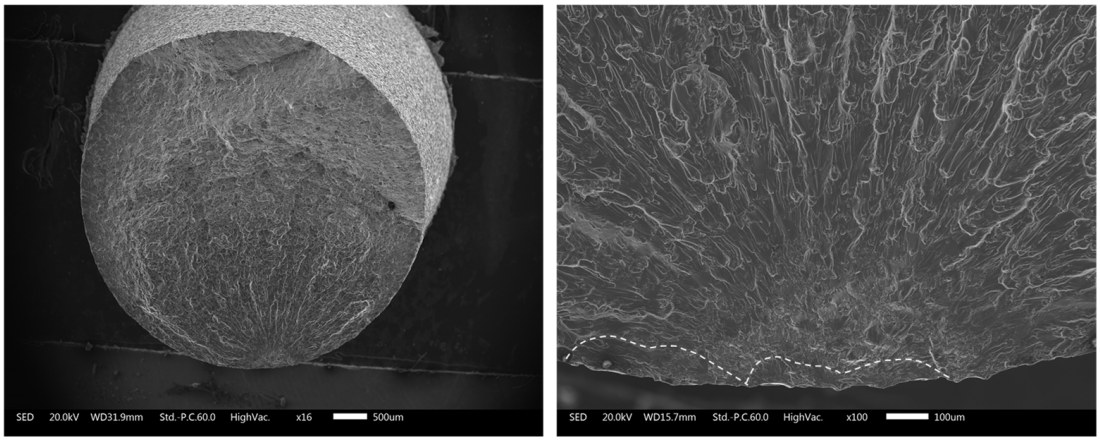


(**a**) (**b**)

**Figure 15.** Fractography of variant Z425 + Z100 subjected to alternating bending stress with amplitude $\sigma_A$ = 220 MPa for 1.8 × $10^5$ cycles and subsequently brought to fracture with axial cyclic testing. (**a**) Fracture surface; (**b**) detail on the initiation site.

The depth dimension of the initial cracks from the surface is, for the shot-peened variants, always lower than the depth of the corresponding residual compressive stress profile. In practice, the fracture still needs to overcome the barrier associated with the residual stress field. It cannot, therefore, be ruled out that in the subsequent phase of life, other cracks may form beneath the surface. This could be related to the more irregular emission spectra observed for several of the shot-peened specimens. It should also be noted that, at this preliminary stage, all these analyses were carried out in the fatigue zone under high-load conditions. Therefore, it cannot be excluded that under high-cycle fatigue conditions, particularly near the upper limit of the fatigue life range investigated, circumstances may arise that promote the initiation of subsurface cracks.

## 4. Conclusions

This work represents an attempt to deepen our understanding of the damage processes that lead to fatigue damage in an Al-alloy component. The analysis of the different shot-peening variants is aimed at studying very different conditions for the initiation and propagation of fatigue cracks, considering the microstructural changes and the different residual stress profiles produced.

Although preliminary, the results obtained for the different variants highlight the potential of the acoustic emission monitoring technique for the early detection of damage initiation. In particular,

- It is possible to see evidence for all experimental variants of a probable crack nucleation relatively early compared to the final fatigue life;
- The AE spectra indicate the probable initiation at about 2/3 of the total life, and therefore a phase of damage accumulation for a non-negligible fraction of the specimen life;
- The final propagation of a dominant crack is accompanied by an intense increase in acoustic emission activity.

The initial stages of damage evolution are not detected by the resonance frequency trend of the test, as the loss of stiffness of the specimen is not sufficient to cause a marked change in the resonance response of the system.

The final increase in acoustic activity clearly overlaps with the loss of stiffness of the specimen, as evidenced by the decrease in test frequency. This confirms the hypothesis that in this last phase, a dominant crack has reached conditions such that its propagation progressively accelerates until fracture.

At present, the variability of the characteristics of the acoustic emission spectra acquired and the limited number of cases available allow us to highlight common behavioral traits but do not allow us to clearly define the differences between the variants studied to obtain a direct correlation between the acoustic emission spectrum and the local state of the material. However, the ability of the method to identify, at least qualitatively, the initial conditions for damage initiation appears very encouraging, as it opens up the possibility of application for the monitoring of components and structures.

**Author Contributions:** Conceptualization, V.F. and M.B. (Matteo Benedetti); methodology, M.B. (Matteo Benedetti), E.R. and V.F.; software, E.R.; validation, M.B. (Matteo Benedetti), V.F. and E.R.; formal analysis, V.F. and P.G.; investigation, M.B. (Matteo Benedetti) and E.R.; resources, M.B. (Michele Bandini); data curation, E.R.; writing—original draft preparation, V.F. and P.G.; writing—review and editing, M.B. (Matteo Benedetti), V.F., E.R., P.G. and M.B. (Michele Bandini); visualization, V.F. and P.G.; supervision, M.B. (Matteo Benedetti); project administration, V.F. All authors have read and agreed to the published version of the manuscript.

**Funding:** This research received no external funding.

**Data Availability Statement:** The original contributions presented in this study are included in the article. Further inquiries can be directed to the corresponding author.

**Acknowledgments:** The authors would like to thank Lorenzo Montanari for his invaluable assistance in conducting the experimental trials and performing the initial data analysis presented in this study.

**Conflicts of Interest:** Author Michele Bandini was employed by PeenService srl. The remaining authors declare that the research was conducted in the absence of any commercial or financial relationships that could be construed as a potential conflict of interest.

## Abbreviation

The following abbreviation is used in this manuscript:

AE Acoustic Emission

## References

1. McClung, R.C. A literature survey on the stability and significance of residual stresses during fatigue. *Fatigue Fract. Eng. Mater. Struct.* **2009**, *30*, 173–205. [CrossRef]
2. Torres, M.A.S.; Voorwald, H.J.C. An evaluation of shot peening, residual stress and stress relaxation on the fatigue life of AISI 4340 steel. *Int. J. Fatigue* **2002**, *24*, 877–886. [CrossRef]

3. Bagheri, S.; Guagliano, M. Review of shot peening processes to obtain nanocrystalline surfaces in metal alloys. *Surf. Eng.* **2009**, *25*, 3–14. [CrossRef]
4. Pariente, I.F.; Guagliano, M. About the role of residual stresses and surface work hardening on fatigue ΔKth of a nitrided and shot peened low-alloy steel. *Surf. Coat. Technol.* **2008**, *202*, 3072–3080. [CrossRef]
5. Soady, K.A. Life assessment methodologies incorporating shot peening process effects: Mechanistic consideration of residual stresses and strain hardening Part 1—Effect of shot peening on fatigue resistance. *Mater. Sci. Technol.* **2013**, *29*, 637–651. [CrossRef]
6. Schubnell, J.; Pontner, P.; Wimpory, R.C.; Farajian, M.; Schulze, V. The influence of work hardening and residual stresses on the fatigue behavior of high frequency mechanical impact treated surface layers. *Int. J. Fatigue* **2020**, *134*, 105450. [CrossRef]
7. Maleki, E.; Unal, O.; Kashyzadeh, K.R. Effects of conventional, severe, over, and re-shot peening processes on the fatigue behavior of mild carbon steel. *Surf. Coat. Technol.* **2018**, *344*, 62–74. [CrossRef]
8. Benedetti, M.; Fontanari, V.; Bandini, M.; Savio, E. High- and very high-cycle plain fatigue resistance of shot peened high-strength aluminum alloys: The role of surface morphology. *Int. J. Fatigue* **2015**, *70*, 451–462. [CrossRef]
9. Bagherifard, S.; Ghelichi, R.; Guagliano, M. Numerical and experimental analysis of surface roughness generated by shot peening. *Appl. Surf. Sci.* **2012**, *258*, 6831–6840. [CrossRef]
10. Marini, M.; Fontanari, V.; Benedetti, M. DEM/FEM simulation of the shot peening process on sharp notches. *Int. J. Mech. Sci.* **2021**, *204*, 106547. [CrossRef]
11. Rodopoulos, C.A.; Curtis, S.A.; de los Rios, E.R.; SolisRomero, J. Optimisation of the fatigue resistance of 2024-T351 aluminium alloys by controlled shot peening—Methodology, results and analysis. *Int. J. Fatigue* **2004**, *26*, 849–856. [CrossRef]
12. Xu, Z.; Dunleavey, J.; Antar, M.; Hood, R.; Soo, S.L.; Kucukturk, G.; Hyde, C.J.; Clare, A.T. The influence of shot peening on the fatigue response of Ti-6Al-4V surfaces subject to different machining processes. *Int. J. Fatigue* **2018**, *111*, 196–207. [CrossRef]
13. Benedetti, M.; Fontanari, V.; Höhn, B.R.; Oster, P.; Tobie, T. Influence of shot peening on bending tooth fatigue limit of case hardened gears. *Int. J. Fatigue* **2002**, *24*, 1127–1136. [CrossRef]
14. Fargas, G.; Roa, J.J.; Mateo, A. Effect of shot peening on metastable austenitic stainless steel. *Mater. Sci. Eng. A* **2015**, *641*, 290–296. [CrossRef]
15. Sheng, J.; Song, L.; Lu, D.; Yang, C.; Liang, Y.; Lin, J. Mechanism of high-cycle fatigue enhancement of TiAl alloys via shot peening. *Int. J. Fatigue* **2026**, *206*, 109420. [CrossRef]
16. ASM International. *ASM Handbook, Volume 2: Properties and Selection Nonferrous Alloys and Special Purpose Materials*; ASM International: Almere, The Netherlands, 1990.
17. Zhao, T.; Jiang, Y. Fatigue of 7075–T651 aluminum alloy. *Int. J. Fatigue* **2008**, *30*, 834–849. [CrossRef]
18. Gao, Y.K. Improvement of fatigue property in 7050–T7451 aluminum alloy by laser peening and shot peening. *Mater. Sci. Eng. A* **2011**, *528*, 3823–3828. [CrossRef]
19. Dursun, T.; Soutis, C. Recent developments in advanced aircraft aluminium alloys. *Mater. Des.* **2014**, *56*, 862–871. [CrossRef]
20. Benedetti, M.; Pedranz, M.; Fontanari, V.; Menapace, C.; Bandini, M. Enhancing plain fatigue strength in aluminum alloys through shot peening: Experimental investigations and a strain energy density interpretation. *Int. J. Fatigue* **2024**, *184*, 108299. [CrossRef]
21. Bagherifard, S. Enhancing the structural performance of lightweight metals by shot peening. *Adv. Eng. Mater.* **2019**, *21*, 1801140. [CrossRef]
22. Benedetti, M.; Bortolamedi, T.; Fontanari, V.; Frendo, F. Bending fatigue behaviour of differently shot peened Al 6082 T5 alloy. *Int. J. Fatigue* **2004**, *26*, 889–897. [CrossRef]
23. Hammond, D.W.; Meguid, S.A. Crack propagation in the presence of shot-peening residual stresses. *Eng. Fract. Mech.* **1990**, *37*, 373–387. [CrossRef]
24. Prasannavenkatesan, R.; Zhang, J.; McDowell, D.L.; Olson, G.B.; Jou, H.-J. 3D modeling of subsurface fatigue crack nucleation potency of primary inclusions in heat treated and shot peened martensitic gear steels. *Int. J. Fatigue* **2009**, *31*, 1176–1189. [CrossRef]
25. Ji, D.; Chen, H.; Zhang, J.; Su, K.; Chen, X. Influence of micro-shot peening and traditional shot peening on fatigue performance and fracture behaviors of Ti-6Al-4V alloy. *Int. J. Fatigue* **2025**, *194*, 108837. [CrossRef]
26. Benedetti, M.; Fontanari, V.; Monelli, B.D. Numerical simulation of residual stress relaxation in shot peened high-strength aluminum alloys under reverse bending fatigue. *J. Eng. Mater. Technol.* **2010**, *132*, 011012. [CrossRef]
27. Qian, W.; Wang, Y.; Liu, K.; Yin, X.; He, X.; Xie, L. Experimental Study on the Effect of Shot Peening and Re-Shot Peening on the Residual Stress Distribution and Fatigue Life of 20CrMnTi. *Coatings* **2023**, *13*, 1210. [CrossRef]
28. Qin, Z.; Li, B.; Zhang, H.; Wilfried, T.Y.A.; Gao, T.; Xue, H. Effects of shot peening with different coverage on surface integrity and fatigue crack growth properties of 7B50-T7751 aluminum alloy. *Eng. Fail. Anal.* **2022**, *133*, 106010. [CrossRef]
29. Oguri, K. Fatigue life enhancement of aluminum alloy for aircraft by Fine Particle Shot Peening (FPSP). *J. Mater. Process. Technol.* **2011**, *211*, 1395–1399. [CrossRef]
30. Chai, M.; Lai, C.; Xu, W.; Duan, Q.; Zhang, Z.; Song, Y. Characterization of Fatigue Crack Growth Based on Acoustic Emission Multi-Parameter Analysis. *Materials* **2022**, *15*, 6665. [CrossRef]

31. Lugo, M.; Jordon, J.B.; Horstemeyer, M.F.; Tschopp, M.A.; Harris, J.; Gokhale, A.M. Quantification of damage evolution in a 7075 aluminum alloy using an acoustic emission technique. *Mater. Sci. Eng. A* **2011**, *528*, 6708–6714. [CrossRef]
32. Vanniamparambil, P.A.; Guclu, U.; Kontsos, A. Identification of crack initiation in aluminum alloys using acoustic emission. *Exp. Mech.* **2015**, *55*, 837–850. [CrossRef]
33. Vi'e, T.; Deschanel, S.; Godin, N.; Normand, B. On the effect of coatings on the tensile and fatigue properties of 7075-T6 aluminum alloy monitored with acoustic Emission (AE): Towards lifetime estimation. *Int. J. Fatigue* **2023**, *171*, 107578. [CrossRef]
34. Sauerbrunn, C.M.; Kahirdeh, A.; Yun, H.; Modarres, M. Damage Assessment Using Information Entropy of Individual Acoustic Emission Waveforms during Cyclic Fatigue Loading. *Appl. Sci.* **2017**, *7*, 562. [CrossRef]
35. Yu, J.; Ziehl, P.; Zárate, B.; Caicedo, J. Prediction of fatigue crack growth in steel bridge components using acoustic emission. *J. Constr. Steel Res.* **2011**, *67*, 1254–1260. [CrossRef]
36. Carpinteri, A.; Lacidogna, G.; Accornero, F.; Mpalaskas, A.C.; Matikas, T.E.; Aggelis, D.G. Influence of damage in the acoustic emission parameters. *Cem. Concr. Compos.* **2013**, *44*, 9–16. [CrossRef]
37. Sagasta, F.; Zitto, M.E.; Piotrkowski, R.; Benavent-Climent, A.; Suarez, E.; Gallego, A. Acoustic emission energy b-value for local damage evaluation in reinforced concrete structures subjected to seismic loadings. *Mech. Syst. Signal Process.* **2018**, *102*, 262–277. [CrossRef]
38. de la Selle, T.; Réthoré, J.; Weiss, J.; Lachambre, J.; Deschanel, S. Signatures of fatigue crack growth from acoustic emission repeaters. *Eng. Fract. Mech.* **2024**, *309*, 110388. [CrossRef]
39. Carrasco, Á.; Méndez, F.; Leaman, F.; Vicuña, C.M. Short review of the use of acoustic emissions for detection and monitoring of cracks. *Acoust. Aust.* **2021**, *49*, 273–280. [CrossRef]
40. Karimian, S.F.; Modarres, M.; Bruck, H.A. A new method for detecting fatigue crack initiation in aluminum alloy using acoustic emission waveform information entropy. *Eng. Fract. Mech.* **2020**, *223*, 106771. [CrossRef]
41. Shan, D.; Nayeb-Hashemi, H. Fatigue-life prediction of SiC particulate reinforced aluminum alloy 6061 matrix composite using AE stress delay concept. *J. Mater. Sci.* **1999**, *34*, 3263–3273. [CrossRef]
42. Russo, F.; Rustighi, E.; Mušálek, R.; Tesař, T.; Fontanari, V.; Rossi, S. Study of damage evolution in 316L stainless steel composite enamel coatings by in situ scanning electron microscopy and acoustic emissions analyses. *Ceram. Int.* **2024**, *50*, 38304–38313. [CrossRef]
43. Ghaib, M.; Shateri, M.; Thomson, D.; Svecova, D. Comparison between microstructural analysis of GFRP and CFRP rebars using micro computed tomography (μCT), scanning electron microscope (SEM), and acoustic emission (AE) techniques. *Compos. Sci. Technol.* **2024**, *250*, 110545. [CrossRef]
44. Wang, Y.; Jia, L.; Chen, Z.; Han, Y.; Jia, L.; Shang, J.; Yan, R. Combining acoustic emission and digital image correlation analysis for dynamic damage response of woven spacer structure reinforced sandwich composites. *Compos. Struct.* **2023**, *319*, 117162. [CrossRef]
45. Almeida, R.S.M.; Magalhães, M.D.; Karim, M.N.; Tushtev, K.; Rezwan, K. Identifying damage mechanisms of composites by acoustic emission and supervised machine learning. *Mater. Des.* **2023**, *227*, 111745. [CrossRef]
46. Physical Acoustics Mistras Group. MICRO80 Product Description. 2023. Available online: https://www.physicalacoustics.com/by-product/sensors/Micro80-200-900-kHz-Miniature-AE-Sensor (accessed on 11 February 2026).